

Dynamic Angle Selection in X-Ray CT: A Reinforcement Learning Approach to Optimal Stopping

Tianyuan Wang

March 18, 2025

1 Abstract

In industrial X-ray Computed Tomography (CT), the need for rapid in-line inspection is critical. Sparse-angle tomography plays a significant role in this by reducing the required number of projections, thereby accelerating processing and conserving resources. Most existing methods aim to balance reconstruction quality and scanning time, typically relying on fixed scan durations. Adaptive adjustment of the number of angles is essential; for instance, more angles may be required for objects with complex geometries or noisier projections. The concept of optimal stopping, which dynamically adjusts this balance according to varying industrial needs, remains underutilized. Building on our previous work, we integrate optimal stopping into sequential Optimal Experimental Design (OED). We propose a novel method for computing the policy gradient within the Actor-Critic framework, enabling the development of adaptive policies for informative angle selection and scan termination. Additionally, we investigated the gap between simulation and real-world applications in the context of the developed learning-based method. Our trained model, developed using synthetic data, demonstrates reliable performance when applied to real-world data. This approach enhances the flexibility of CT operations and expands the applicability of sparse-angle tomography in industrial settings.

2 Introduction

X-ray Computed Tomography (CT) enables inline industrial inspection through three-dimensional reconstruction. However, fast and adaptive CT scanning is essential to make its widespread industrial application feasible. Previous studies have shown that not all projections are equally informative for certain objects [1, 2]. Most research has focused on sequentially selecting informative angles to enhance efficiency. This sequential Optimal Experimental Design (OED) is often described within a Bayesian framework [3, 4, 5], where angles are chosen to maximize information gain. Information gain is typically quantified by comparing the prior and posterior distributions of the reconstruction or by assessing the similarity between the reconstructed image and the ground truth.

Batenburg *et al.* [6] and Dabravolski *et al.* [7] used a set of template images composed of Gaussian blobs to represent samples from the prior distribution. They introduced an upper bound [8] to approximate the information gain, which reflects the diameter of the solution set. Burger *et al.* [9] employed classical “alphabetic criteria” for OED, such as “A-” and “D-” optimality, using the trace or determinant of the covariance matrix of the posterior distribution as summary statistics [10]. Additionally, they used a Gaussian distribution as a prior, updating the posterior after selecting each angle. Building on this approach, Helin [11] introduced a Total Variation (TV) prior to enhance edges in reconstructions. The non-Gaussian TV prior was approximated as a Gaussian distribution using lagged diffusivity iteration. Furthermore, Barbano [12] utilized a deep image prior as the reconstruction method and linearized the network to approximate the posterior distribution as a Gaussian. To avoid the need for a closed-form solution, Elata *et al.* [13] proposed using a diffusion model for CT reconstruction, sampling from the posterior to approximate the posterior covariance matrix.

Recently, policy-based methods from the reinforcement learning community have been introduced into sequential OED [14, 15, 16]. In the medical CT field, Shen *et al.* [17] trained a gated recurrent unit as a policy network on simulated medical data to map projections to probabilities over the angle space. Wang *et al.* [18] explored industrial CT applications with very few angles, transitioning from simple to complex shapes. They trained a policy that maps the current reconstruction to probabilities over the angle space. Additionally, Wang *et al.* [19] addressed a specific task—defect detection—by incorporating an extra reward for defect detectability and prior information about defects, enabling the trained policy to identify informative angles to aid in defect detection.

While there has been significant research on identifying informative angles, the optimal selection of the number of angles has often been overlooked. Additionally, most studies have focused on simulated data rather than real-world data. This is particularly evident in learning-based methods, which rely on training with simulated data, leaving their generalizability to real-world data uncertain.

The contributions of this work include the development of an optimal stopping method to balance the trade-off between experimental costs and experimental goals, such as reconstruction quality. This approach enables both adaptive selection of informative angles and optimal scan termination based on experimental costs. By incorporating a terminal policy into the Actor-Critic framework, we proposed a novel method for computing the policy gradient, jointly optimizing angle selection and the terminal policy. Additionally, we investigated the gap between simulation and real-world applications by evaluating the trained model on real data.

The structure of the paper is as follows: The Background section provides an overview of the fundamental concepts and notations related to inverse problems and sequential OED using reinforcement learning. The Method section introduces our novel approach for computing the policy gradient. The Results section presents the findings from both simulation and real-world data experiments. Finally, the paper concludes with a discussion of the key findings and their implications.

3 Background

3.1 Inverse Problem

In the context of the forward problem, measurements $\mathbf{y}(\boldsymbol{\theta})$ are obtained from the underlying parameters $\bar{\mathbf{x}}$ using a forward operator $\mathbf{A}(\boldsymbol{\theta})$, which is determined by the design parameters $\boldsymbol{\theta} = \{\theta_1, \dots, \theta_M\}$. In the case of X-ray CT, the forward operator $\mathbf{A}(\boldsymbol{\theta})$ corresponds to the Radon transform for angles $\boldsymbol{\theta}$. Since the measurement process is subject to noise, we also incorporate a noise term $\boldsymbol{\epsilon}(\boldsymbol{\theta})$ and model the projections as follows:

$$\mathbf{y}(\boldsymbol{\theta}) = \mathbf{A}(\boldsymbol{\theta})\bar{\mathbf{x}} + \boldsymbol{\epsilon}(\boldsymbol{\theta}). \quad (1)$$

The inverse problem involves using the projections $\mathbf{y}(\boldsymbol{\theta})$ and the forward operator $\mathbf{A}(\boldsymbol{\theta})$ to reconstruct the underlying parameters $\bar{\mathbf{x}}$, denoted as $\hat{\mathbf{x}}(\boldsymbol{\theta})$. However, solving inverse problems is often challenging due to their ill-posedness [20]. The accuracy of the reconstructed underlying parameters is influenced by the design parameters $\boldsymbol{\theta}$, making their optimal selection crucial. OED is employed to select the most informative angles to acquire the corresponding projections. To quantify the accuracy of the reconstruction, a utility function is defined within the OED framework. The optimal design $\boldsymbol{\theta}^*$ is then obtained by maximizing the expected value of this utility function over the design space, taking into account the projections $\mathbf{y}(\boldsymbol{\theta})$ and the underlying parameters $\bar{\mathbf{x}}$ [3, 21].

3.2 Sequential Optimal Experimental Design (OED) and Reinforcement Learning

OED seeks to infer underlying parameters $\bar{\mathbf{x}}$ with minimal experimental costs by selecting informative design parameters [4, 21]. Traditional experimental design assumes that the underlying parameters are static, with optimal design parameters selected simultaneously. This approach neglects the feedback obtained after each design parameter is chosen [14], which could influence subsequent selections.

Sequential OED extends the concept of traditional OED by allowing the design parameters to be determined sequentially, based on the data acquired from previous projections, rather than selecting all design parameters simultaneously [14, 5]. For example, the design parameter θ_k can be chosen based on the previous projections $\mathbf{y}(\{\theta_1, \dots, \theta_{k-1}\})$. This approach enables the design process to adapt dynamically to changes in the underlying parameters by adjusting the design parameters iteratively.

The OED process for solving inverse problems is inherently a bi-level optimization problem, often characterized by its non-convex, non-linear, and high-dimensional nature, particularly in imaging reconstruction [22]. The sequential approach further complicates this optimization, as the bi-level optimization problem would need to be solved in real time. Reinforcement Learning (RL), a machine learning technique designed for fast sequential decision-making, facilitates the resolution of this sequential OED by training through interaction with the environment. RL is grounded in the framework of Markov Decision Processes (MDP), which consist of a state space, action space, transition model, and reward function. In practice, MDPs are sometimes extended to Partially Observable MDPs (POMDPs) when the underlying state is not fully observable, necessitating the reconstruction of the belief state from measurements. The goal of RL is to learn a parameterized policy that maps the current state to the next action, maximizing the expectation of the cumulative rewards [23].

In the context of sequential OED, at the k^{th} step, the reconstructed underlying parameters $\hat{\mathbf{x}}_k$, inferred from all previous projections $\mathbf{y}(\{\theta_1, \dots, \theta_{k-1}\})$, serve as the belief state. The action space corresponds to the design parameter, and the utility function used for accuracy estimation

acts as the reward function R . For example, R can be defined as the Peak Signal-to-Noise Ratio (PSNR), which estimates the reconstruction quality by comparing the reconstruction with the ground truth [18]. Consequently, the optimization problem of sequential OED is reformulated as learning a parameterized policy $\pi_{\text{action}}(\theta_k|\hat{\mathbf{x}}_k; \mathbf{w}_a)$, where \mathbf{w}_a represents the policy parameters. This policy, with the optimal parameters \mathbf{w}_a^* , maximizes the expectation of the cumulative utilities obtained from the experiments.

By employing RL, the optimization process is simplified by focusing on optimizing the policy parameters rather than directly optimizing the design parameters. The state-value function $V^{\pi_a}(\hat{\mathbf{x}}_1)$ represents the expected cumulative reward starting from the initial state $\hat{\mathbf{x}}_1$ and following the distribution π_{chain} . This distribution is defined as the product of the action selection policy $\pi_{\text{action}}(\theta_k|\hat{\mathbf{x}}_k; \mathbf{w}_a)$ and the transition model $\pi_t(\hat{\mathbf{x}}_{k+1}|\hat{\mathbf{x}}_k, \theta_k)$. Formally, the state-value function is expressed as:

$$V^{\pi_a}(\hat{\mathbf{x}}_1) = \mathbb{E}_{\boldsymbol{\tau} \sim \pi_{\text{chain}}} \left[\sum_{k=1}^M r_k \mid \hat{\mathbf{x}}_1 \right], \quad (2)$$

and the chain distribution is given by

$$\pi_{\text{chain}}(\boldsymbol{\tau}; \mathbf{w}_a) = \prod_{k=1}^M \pi_{\text{action}}(\theta_k|\hat{\mathbf{x}}_k; \mathbf{w}_a) \pi_t(\hat{\mathbf{x}}_{k+1}|\hat{\mathbf{x}}_k, \theta_k). \quad (3)$$

Here, a trajectory $\boldsymbol{\tau}$ of M steps, $\{\hat{\mathbf{x}}_1, (\theta_1, \hat{\mathbf{x}}_2, r_1), (\theta_2, \hat{\mathbf{x}}_3, r_2), \dots, (\theta_M, \hat{\mathbf{x}}_{M+1}, r_M)\}$, is sampled from π_{chain} . Starting from the initial state $\hat{\mathbf{x}}_1$, each step involves selecting a design parameter θ_k , transitioning to the next state $\hat{\mathbf{x}}_{k+1}$, and accumulating the reward r_k .

The objective is to maximize the expected cumulative rewards across the trajectory. For a fixed initial state $\hat{\mathbf{x}}_1$, the objective function of RL can be expressed in terms of the state-value function as:

$$J(\mathbf{w}_a) = V^{\pi_a}(\hat{\mathbf{x}}_1). \quad (4)$$

The value function can also be linked to actions through the action-state value function $Q^{\pi_a}(\hat{\mathbf{x}}, \theta)$, which estimates the expected cumulative rewards at the current state and specific action. The relationship between the state-value function and the action-value function is given by:

$$V^{\pi_a}(\hat{\mathbf{x}}) = \sum_{\theta} \pi_{\text{action}}(\theta|\hat{\mathbf{x}}; \mathbf{w}_a) Q^{\pi_a}(\hat{\mathbf{x}}, \theta). \quad (5)$$

The advantage function quantifies how much better a specific action is compared to the average performance at a given state. It is defined as:

$$A^{\pi_a}(\hat{\mathbf{x}}, \theta) = Q^{\pi_a}(\hat{\mathbf{x}}, \theta) - V^{\pi_a}(\hat{\mathbf{x}}). \quad (6)$$

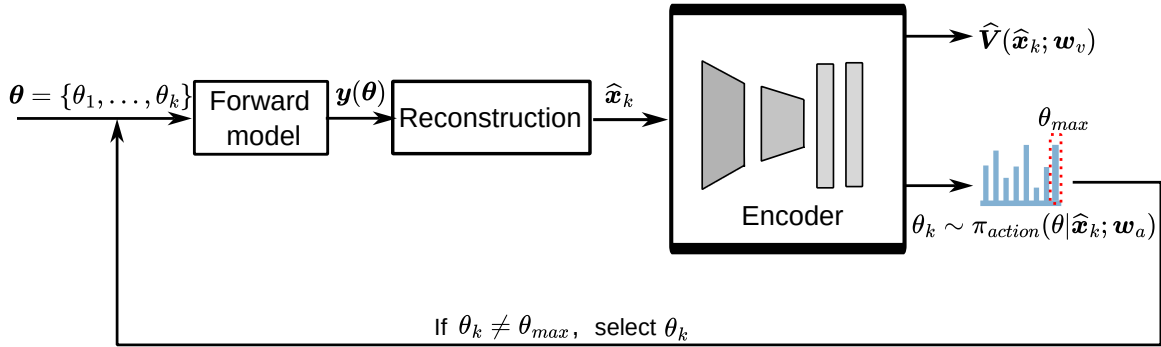
4 Method

4.1 Naive optimal stopping

Optimal stopping for sequential OED can be implemented by introducing an additional terminal action within the action space. The *reward function* for 'termination' and 'continuation' is defined by $R(\hat{\mathbf{x}}, \bar{\mathbf{x}}, \theta)$, which accounts for the decision to either continue or terminate, as follows::

$$R(\hat{\mathbf{x}}, \bar{\mathbf{x}}, \theta) = \begin{cases} -b, & \text{if } \theta = \theta_{max}, \\ \text{PSNR}(\hat{\mathbf{x}}, \bar{\mathbf{x}}), & \text{if otherwise,} \end{cases}$$

where $\text{PSNR}(\hat{\mathbf{x}}, \bar{\mathbf{x}})$ is a function that serves as the immediate reward, evaluating the quality of the experiment at the stopping point $\hat{\mathbf{x}}$, and $-b$ is a negative scaling factor representing the experimental cost incurred at each step.



(a) Naive optimal stopping

Figure 1: This figure illustrates the workflow of the naive optimal stopping algorithm.

As described in our previous work [18] and shown in Figure 1, after selecting k angles $\theta = \{\theta_1, \dots, \theta_k\}$, the *observations* $\mathbf{y}(\theta)$ are obtained from the forward operator. The reconstructed image $\hat{\mathbf{x}}_k$ is then used as the *belief state* and serves as the input to the shared encoder (initial belief state $\hat{\mathbf{x}}_1$ is a zero matrix), which has multi-head outputs. The shared encoder has two branches. One branch is designed to estimate the state-value function $V^{\pi_a}(\hat{\mathbf{x}})$, and we use $\hat{V}(\hat{\mathbf{x}}; \mathbf{w}_v)$ for this approximation, where \mathbf{w}_v denotes the neural network parameters. The other branch outputs the distribution over the *action space*, which consists of all possible angles and the terminal probability θ_{max} as the final action. The inclusion of a mixture of actions for angles and termination represents the primary difference from the standard method described in our previous work [18]. Consequently, the Temporal Difference (TD) error [23] for the terminal action is modified to account for the reward at the termination state $\text{PSNR}(\hat{\mathbf{x}}_{k+1}, \bar{\mathbf{x}})$, as shown in line 10 of Algorithm (1). Algorithm (1) outlines the modified algorithm based on the previous work [18].

Algorithm 1

for each episode do:

2: Initialize the action policy parameters \mathbf{w}_a , and the value function parameters \mathbf{w}_v randomly. Define the maximal experimental steps M . Set step sizes $\alpha^{\mathbf{w}_a} > 0$, $\alpha^{\mathbf{w}_v} > 0$, and $n = 0$. A zero matrix serves as the initial state $\hat{\mathbf{x}}_1$.

while $\theta_k \neq \theta_{\max}$ **and** $k < M$:

4: Select the angle based on the Soft-max policy, which maps the inputs to a probability distribution that sums to 1: $\theta_k \sim \pi_{\text{action}}(\theta|\hat{\mathbf{x}}_k; \mathbf{w}_a)$
 Get new measurements \mathbf{y}_k from the forward operator

6: Reconstruct new image $\hat{\mathbf{x}}_{k+1}$
 Get reward for continuation $-b$, and reward for termination $\text{PSNR}(\hat{\mathbf{x}}_{k+1}, \bar{\mathbf{x}})$

8: Estimate the state-values $\hat{V}(\hat{\mathbf{x}}_k; \mathbf{w}_v)$ and $\hat{V}(\hat{\mathbf{x}}_{k+1}; \mathbf{w}_v)$
 Compute TD error:
 if $\theta_k = \theta_{\max}$:
 $\delta_k = -b + \text{PSNR}(\hat{\mathbf{x}}_{k+1}, \bar{\mathbf{x}}) - \hat{V}(\hat{\mathbf{x}}_k; \mathbf{w}_v)$
 else:
 $\delta_k = -b + \hat{V}(\hat{\mathbf{x}}_{k+1}; \mathbf{w}_v) - \hat{V}(\hat{\mathbf{x}}_k; \mathbf{w}_v)$

10: Update the action policy function parameters \mathbf{w}_a :
 $\mathbf{w}_a \leftarrow \mathbf{w}_a + \alpha^{\mathbf{w}_a} \nabla_{\mathbf{w}_a} \log \pi_{\text{action}}(\theta_k|\hat{\mathbf{x}}_k; \mathbf{w}_a) \delta_k$
 Update value function parameters \mathbf{w}_v :
 $\mathbf{w}_v \leftarrow \mathbf{w}_v + \alpha^{\mathbf{w}_v} \nabla_{\mathbf{w}_v} \hat{V}(\hat{\mathbf{x}}_k; \mathbf{w}_v) \delta_k$

12: Increase the step number $k += 1$

end for

4.2 Optimal stopping using terminal policy

4.2.1 Objective function

Different from the naive optimal stopping, we consider an independent parameterized terminal policy [24], which maps the state $\hat{\mathbf{x}}$ to a stochastic stopping decision $d \sim \pi_{\text{ter}}(d|\hat{\mathbf{x}}; \mathbf{w}_t)$. The continuation corresponds to $d = 0$, while termination corresponds to $d = 1$. Apart from the stopping decision, the reward function remains the same as in naive optimal stopping.

In the context of optimal stopping for sequential OED, the framework integrates both the terminal policy for scan termination and the action policy for angle selection, instead of combining them within the same action space as in the naive approach. First, we reformulate the probability chain from Equation (3) to incorporate the termination decision. The updated probability chain reflects the decision-making process of the terminal policy, which evaluates at each step whether the trajectory should terminate or continue. First, we define a portion of the probability chain as:

$$\pi_{\text{sec}}(d, \hat{\mathbf{x}}', \theta|\hat{\mathbf{x}}; \mathbf{w}_a, \mathbf{w}_t) = \pi_{\text{ter}}(d|\hat{\mathbf{x}}; \mathbf{w}_t) + \left(1 - \pi_{\text{ter}}(d|\hat{\mathbf{x}}; \mathbf{w}_t)\right) \pi_{\text{policy}}(\theta|\hat{\mathbf{x}}; \mathbf{w}_a) \pi_t(\hat{\mathbf{x}}'|\hat{\mathbf{x}}, \theta). \quad (7)$$

Similar to Equation (3), the probability chain $\pi_{\text{Cchain}}(\tau_C; \mathbf{w}_a, \mathbf{w}_t)$ with the inclusion of the termination distribution is expressed as:

$$\pi_{\text{Cchain}}(\tau_C; \mathbf{w}_a, \mathbf{w}_t) = \prod_{k=1}^T \pi_{\text{sec}}(d_k, \hat{\mathbf{x}}_{k+1}, \theta_k|\hat{\mathbf{x}}_k; \mathbf{w}_a, \mathbf{w}_t), \quad (8)$$

The stopping step T is determined by the terminal policy, which is less or equal to the maximal step M and $d_M \equiv 1$. A trajectory up to the stopping point is generated from the new π_{Cchain} as:

$$\{\hat{\mathbf{x}}_1, (d_1, \theta_1, \hat{\mathbf{x}}_2, -b), (d_2, \theta_2, \hat{\mathbf{x}}_3, -b), \dots, (d_T, \theta_T, \hat{\mathbf{x}}_{T+1}, p_T)\}.$$

This trajectory represents the sequence of states ($\hat{\mathbf{x}}$), termination indicators (d), negative reward ($-b$), and quality evaluations $\text{PSNR}(\hat{\mathbf{x}}_T, \bar{\mathbf{x}})$ (p_T) at termination. The process is designed to terminate at step T as soon as $d_T = 1$, ensuring that the trajectory is finite and explicitly concludes. For all prior steps ($i < T$), $d_i = 0$, indicating that the process continues during those steps.

The objective function, representing the value function at the fixed initial state $\hat{\mathbf{x}}_1$, aims to learn both the action and terminal policies that maximize the expected cumulative rewards:

$$\begin{aligned} J(\mathbf{w}_a, \mathbf{w}_t) &= V^{\pi_a, \pi_t}(\hat{\mathbf{x}}_1) \\ &= \pi_{\text{ter}}(d_1 | \hat{\mathbf{x}}_1; \mathbf{w}_t) \text{PSNR}(\hat{\mathbf{x}}_1, \bar{\mathbf{x}}) \\ &\quad + \left(1 - \pi_{\text{ter}}(d_1 | \hat{\mathbf{x}}_1; \mathbf{w}_t)\right) V_C^{\pi_a, \pi_t}(\hat{\mathbf{x}}_1). \end{aligned} \quad (9)$$

Here, the continuation state-value function is defined as follows [25, 26]:

$$V_C^{\pi_a, \pi_t}(\hat{\mathbf{x}}_1) = -b + \mathbb{E}_{\tau_C^{(2)} \sim \pi_{\text{Cchain}}^{(2)}} [V^{\pi_a, \pi_t}(\hat{\mathbf{x}}_2)], \quad (10)$$

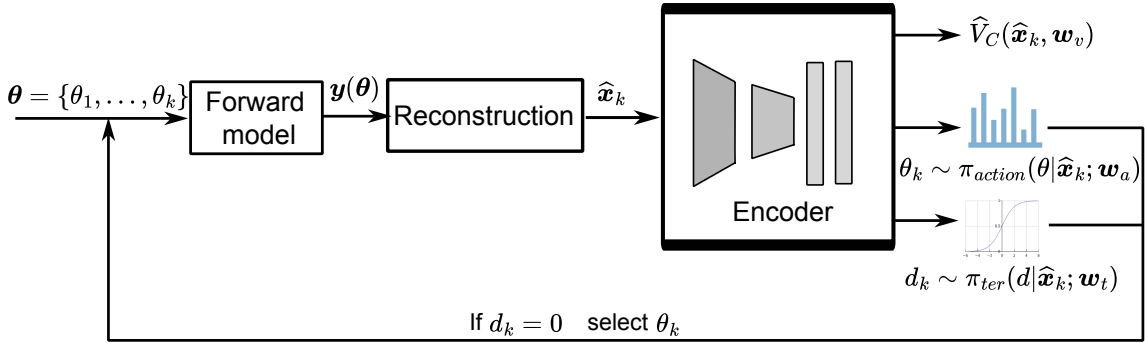
where $\tau_C^{(2)}$ represents the trajectory starting from $\hat{\mathbf{x}}_2$, following the probability chain described in Equation (8).

Similarly, the continuation action-value function is defined only when the trajectory continues, as one of its inputs is the action: $Q_C^{\pi_a, \pi_t}(\hat{\mathbf{x}}, \theta)$.

The optimal terminal policy $\pi_{\text{ter}}^*(d_k | \hat{\mathbf{x}}_k; \mathbf{w}_t)$ at step k is defined as [27, 28, 25]:

$$\pi_{\text{ter}}^*(d_k | \hat{\mathbf{x}}_k; \mathbf{w}_t) = \begin{cases} \mathbb{I}(\text{PSNR}(\hat{\mathbf{x}}_k, \bar{\mathbf{x}}) \geq V_C^{\pi_a, \pi_t}(\hat{\mathbf{x}}_k)), & \text{if } k < M, \\ 1, & \text{if } k = M, \end{cases} \quad (11)$$

where $\mathbb{I}(\cdot)$ denotes the indicator function and M is the maximum number of steps in the experiment.



(b) Optimal stopping using terminal policy

Figure 2: This figure illustrates the workflow of the optimal stopping using terminal policy.

Figure (2) illustrates the workflow of optimal stopping using the terminal policy. Compared to the naive optimal stopping, this approach includes an additional branch for the terminal policy, which uses the sample from Sigmoid function to determine continuation or termination. Another distinction is that one branch estimates the continuation value function $V_C^{\pi_a, \pi_t}(\hat{\mathbf{x}}_k)$ using $\hat{V}_C(\hat{\mathbf{x}}_k, \mathbf{w}_v)$.

4.2.2 Policy gradient

To jointly solve the optimal stopping and action selection problems for sequential OED, we propose a novel policy gradient method. The policy gradients are calculated using Equation (9).

For the gradient with respect to the action policy \mathbf{w}_a , the detailed unrolling recursive derivation is provided in Appendix A. By sampling from N trajectories, the gradient is expressed as:

$$\begin{aligned} \nabla_{\mathbf{w}_a} J(\mathbf{w}_a, \mathbf{w}_t) &= \nabla_{\mathbf{w}_a} V^{\pi_a, \pi_t}(\hat{\mathbf{x}}_1) \\ &\approx \sum_{n=1}^N \left(\sum_{k=1}^T \nabla_{\mathbf{w}_a} \log \pi_{\text{action}}(\theta_k | \hat{\mathbf{x}}_k; \mathbf{w}_a) Q_C^{\pi_a, \pi_t}(\hat{\mathbf{x}}_k, \theta) \right), \end{aligned} \quad (12)$$

To improve the stability and efficiency of action policy gradient computation, a baseline is introduced by replacing the action-state value function in Equation (12) with an advantage function [23]. The continuation advantage function is defined by incorporating the output of the terminal policy; further details are provided in Appendix A. The continuation advantage function is approximated as:

$$\begin{aligned} A_C^{\pi_a, \pi_t}(\hat{\mathbf{x}}, \theta) &\approx -b + \left(1 - \pi_{\text{ter}}(d' | \hat{\mathbf{x}}'; \mathbf{w}_t)\right) V_C^{\pi_a, \pi_t}(\hat{\mathbf{x}}') \\ &\quad + \pi_{\text{ter}}(d' | \hat{\mathbf{x}}'; \mathbf{w}_t) \text{PSNR}(\hat{\mathbf{x}}', \bar{\mathbf{x}}) - V_C^{\pi_a, \pi_t}(\hat{\mathbf{x}}). \end{aligned} \quad (13)$$

We perform stochastic gradient ascent to update the parameters of the angle policy, \mathbf{w}_a , using a step size of $\alpha^{\mathbf{w}_a}$.

$$\mathbf{w}_a \leftarrow \mathbf{w}_a + \alpha^{\mathbf{w}_a} \nabla_{\mathbf{w}_a} \log \pi_{\text{action}}(\theta | \hat{\mathbf{x}}; \mathbf{w}_a) A_C^{\pi_a, \pi_t}(\hat{\mathbf{x}}, \theta) \quad (14)$$

For the gradient with respect to the terminal policy \mathbf{w}_t , the detailed unrolling recursive derivation is provided in Appendix B. By sampling from N trajectories, the gradient is expressed as:

$$\begin{aligned} \nabla_{\mathbf{w}_t} J(\mathbf{w}_a, \mathbf{w}_t) &= \nabla_{\mathbf{w}_t} V^{\pi_a, \pi_t}(\hat{\mathbf{x}}) \\ &\approx \sum_{n=1}^N \left(\sum_{k=1}^T \nabla_{\mathbf{w}_t} \pi_{\text{ter}}(d_k | \hat{\mathbf{x}}_k; \mathbf{w}_t) \left(\text{PSNR}(\hat{\mathbf{x}}_k, \bar{\mathbf{x}}) - V_C^{\pi_a, \pi_t}(\hat{\mathbf{x}}_k) \right) \right), \end{aligned} \quad (15)$$

We also perform stochastic gradient ascent to update the parameters of the terminal policy, \mathbf{w}_t , using a step size of $\alpha^{\mathbf{w}_t}$.

$$\mathbf{w}_t \leftarrow \mathbf{w}_t + \alpha^{\mathbf{w}_t} \nabla_{\mathbf{w}_t} \pi_{\text{ter}}(d | \hat{\mathbf{x}}; \mathbf{w}_t) \left(\text{PSNR}(\hat{\mathbf{x}}, \bar{\mathbf{x}}) - V_C^{\pi_a, \pi_t}(\hat{\mathbf{x}}) \right) \quad (16)$$

The complete algorithm is presented in Algorithm (2).

Algorithm 2

```
1: for each episode do:
2: Initialize the action policy parameters  $\mathbf{w}_a$ , the terminal policy parameters  $\mathbf{w}_t$ , and the value
   function parameters  $\mathbf{w}_v$  randomly. Define the maximal experimental steps  $M$ . Set step sizes
    $\alpha^{\mathbf{w}_a} > 0$ ,  $\alpha^{\mathbf{w}_t} > 0$ ,  $\alpha^{\mathbf{w}_v} > 0$ , and  $n = 0$ . A zero matrix serves as the initial state  $\hat{\mathbf{x}}_1$ .  $d_1 \sim$ 
    $\pi_{\text{ter}}(d|\hat{\mathbf{x}}_1; \mathbf{w}_t)$ .
3:   while  $d_k = 0$  and  $k < M$ :
4:     Select the angle based on the Soft-max policy, which maps the inputs
       to a probability distribution that sums to 1:  $\theta_k \sim \pi_{\text{policy}}(\theta|\hat{\mathbf{x}}_k; \mathbf{w}_a)$ 
5:     Get new measurements  $\mathbf{y}_k$  from the forward operator
6:     Reconstruct new image  $\hat{\mathbf{x}}_{k+1}$ 
7:     Get reward for continuation  $-b$ , and rewards for termination  $\text{PSNR}(\hat{\mathbf{x}}_k, \bar{\mathbf{x}})$ 
       and  $\text{PSNR}(\hat{\mathbf{x}}_{k+1}, \bar{\mathbf{x}})$ 
8:     Determine the terminal action based on the Sigmoid policy, which
       maps the inputs to terminal probability:  $d_k \sim \pi_{\text{ter}}(d|\hat{\mathbf{x}}_k; \mathbf{w}_t)$ 
9:     Estimate the state-values  $\hat{V}_C(\hat{\mathbf{x}}_k; \mathbf{w}_v)$  and  $\hat{V}_C(\hat{\mathbf{x}}_{k+1}; \mathbf{w}_v)$ 
10:    Compute TD error:  $\delta_k = -b + \left(1 - \pi_{\text{ter}}(d_{k+1}|\hat{\mathbf{x}}_{k+1}; \mathbf{w}_t)\right)\hat{V}_C(\hat{\mathbf{x}}_{k+1}; \mathbf{w}_v)$ 
        $+ \pi_{\text{ter}}(d_{k+1}|\hat{\mathbf{x}}_{k+1}; \mathbf{w}_t)\text{PSNR}(\hat{\mathbf{x}}_{k+1}, \bar{\mathbf{x}}) - \hat{V}_C(\hat{\mathbf{x}}_k; \mathbf{w}_v)$ 
11:    Update policy function parameters  $\mathbf{w}_a$ :
        $\mathbf{w}_a \leftarrow \mathbf{w}_a + \alpha^{\mathbf{w}_a} \nabla_{\mathbf{w}_a} \log \pi_{\text{action}}(\theta_k|\hat{\mathbf{x}}_k; \mathbf{w}_a) \delta_k$ 
12:    Update policy function parameters  $\mathbf{w}_t$ :
        $\mathbf{w}_t \leftarrow \mathbf{w}_t + \alpha^{\mathbf{w}_t} \nabla_{\mathbf{w}_t} \pi_{\text{ter}}(d_k|\hat{\mathbf{x}}_k; \mathbf{w}_t) \left(\text{PSNR}(\hat{\mathbf{x}}_k, \bar{\mathbf{x}}) - \hat{V}_C(\hat{\mathbf{x}}_k; \mathbf{w}_v)\right)$ 
13:    Update value function parameters  $\mathbf{w}_v$ :
        $\mathbf{w}_v \leftarrow \mathbf{w}_v + \alpha^{\mathbf{w}_v} \nabla_{\mathbf{w}_v} \hat{V}_C(\hat{\mathbf{x}}_k; \mathbf{w}_v) \delta_k$ 
14:    Increase the step number  $k += 1$ 
15: end for
```

5 Results

The proposed optimal stopping method for sequential OED was validated through a series of X-ray CT experiments. These experiments demonstrated the method’s capability to adaptively determine the optimal number of angles based on the object’s shape and noise levels, as well as to perform accurate adaptive informative angles selection. The model was first trained using synthetic data and then evaluated on real-world data to test its performance and generalizability.

5.1 Dataset

5.1.1 Synthetic dataset

We analyzed a synthetic dataset that features well-known informative angles. The dataset includes three shapes—parallelograms, triangles, and pentagons—each varying in scale, rotation, and position. These variations result in differing requirements for the number of angles needed to achieve accurate reconstructions. Figure (3) provides example images from this dataset, while the parameters used for its generation are outlined in the Appendix.

For training on the synthetic data, the Astra Toolbox [29, 30] was used to generate the simulated projections. For the reconstruction tasks involving training on synthetic data and testing on real

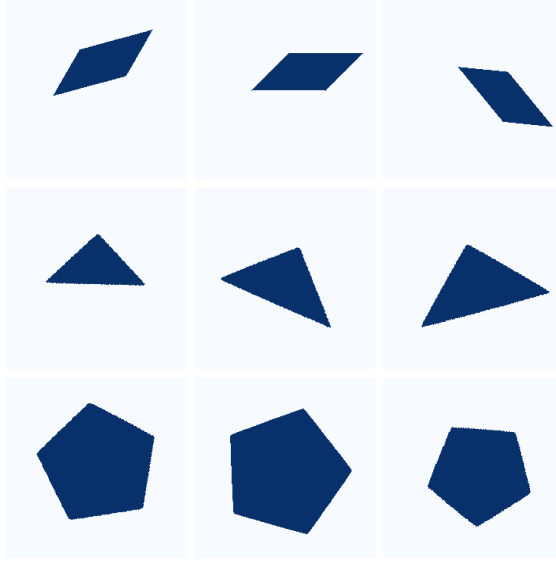


Figure 3: The figure shows nine samples from the synthetic dataset, including parallelograms, triangles, and pentagons. Each shape type is represented by three samples.

data, the SIRT algorithm with a non-negativity constraint was applied for 150 iterations.

5.1.2 Real dataset

All data were collected at the FleX-ray laboratory of Centrum Wiskunde en Informatica (CWI) in Amsterdam, the Netherlands [31]. A Region-of-Interest (ROI) scanning approach was used to acquire projections with dimensions of 956×10 pixels. The source-to-object and detector-to-object distances were both set to 225 mm. An exposure time of 80 ms per projection was applied, and the source spectrum was shaped using filters consisting of 0.1 mm zinc, 0.2 mm copper, and 0.5 mm aluminum. A total of 3601 projections were acquired. Figure (4) illustrates the scanning setup.

The dataset consists of two laser-cut objects made from a 6-mm-thick transparent plastic material called acrylate. The objects have triangular and pentagonal shapes, each containing 12 samples with varying sizes. The right-angle edges of the triangular samples range from 2.8 cm to 4.0 cm, while the edges of the pentagonal samples range from 2.5 cm to 3.0 cm. Each scanning session involved different placements of the objects, resulting in variations in rotation and translation. To create a dataset with two noise levels, two emission currents were used: $600 \mu\text{A}$ and $100 \mu\text{A}$. The lower emission current ($100 \mu\text{A}$) produced data with higher noise levels. Finally, 12 groups of projections were acquired for each shape and each noise level, resulting in a total of 48 groups of projections.

After data acquisition, the number of projections was reduced to 361 by subsampling every 10th projection. To approximate the cone-beam geometry as a fan-beam geometry, only the middle row of the detector was used. The column size of the projections was then reduced to 239 by selecting every fourth pixel on the detector. Furthermore, the fan-beam geometry was transformed into a parallel-beam geometry with 180 projections to simplify angle selection [32]. This transformation made it easier to identify the informative angles, as they are tangential to the edges in parallel-beam geometry.

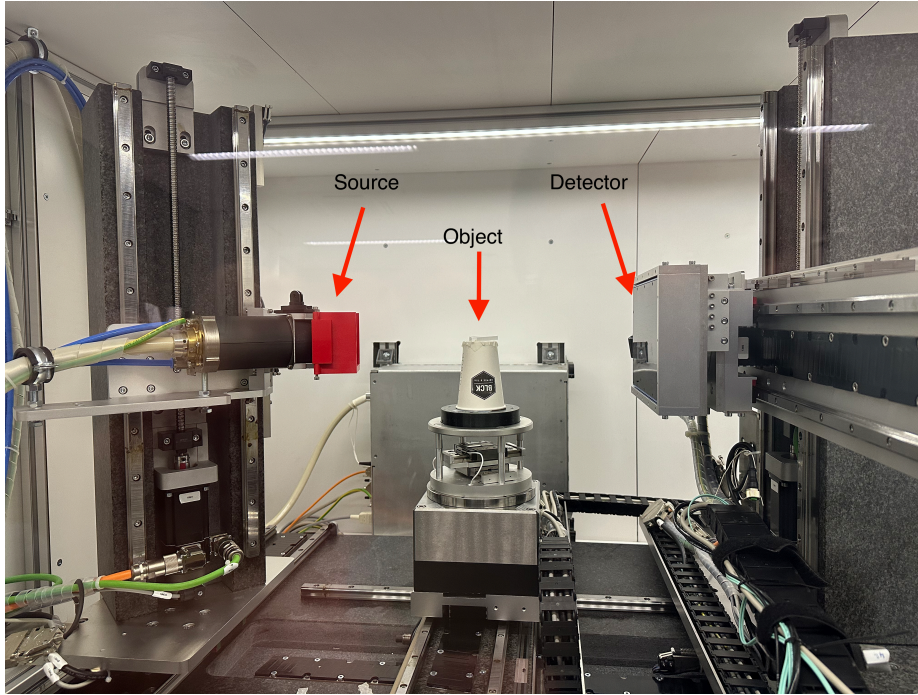


Figure 4: The scanning setup at the FleX-ray laboratory, with the object to be scanned placed on a paper cup for positioning.

5.2 Implementation

For the algorithm implementation, the architectures of the encoder and the Actor-Critic neural networks are detailed in the Appendix. During training, weights of 1.0 and 0.5 were assigned to the actor loss and critic loss in Algorithm (1) and Algorithm (2), respectively. To encourage exploration during training, an entropy loss with a weight of 0.01 was included. Compared to Algorithm (1), Algorithm (2) included an additional loss term for the terminal policy with a weight of 1.0. These parameter settings were empirically chosen to strike an optimal balance between policy optimization, accurate value estimation, and robust exploration during training. The parameters were optimized using the Adam optimizer [33] with a learning rate of 10^{-4} and a weight decay of 10^{-5} .

5.3 Training on synthetic data with Gaussian noise

In this experiment, we investigated whether the two algorithms could adaptively determine the optimal number of angles for CT imaging by adjusting the reward values before termination. The projections incorporated 5% Gaussian noise. For Algorithms (1) and (2), the reward values ranged from -0.4 to -0.9 in intervals of 0.1. The variation in reward value ranges indicated that higher experimental costs shifted the trade-off between image quality and the number of projections. A separate model was trained for each reward value using the synthetic dataset shown in Figure (3). To prevent excessively non-termination during training, the maximum number of angles, M , in line 3 of Algorithm (1) and Algorithm (2), was limited to 20.

During training, each episode involved sampling a data point from the dataset shown in Figure

(3). The policy was trained at each angle selection step until termination, thereby completing the episode. A total of 80,000 episodes (i.e., 80,000 sampled data points) were considered. However, the naive stopping mechanism from Algorithm (1) failed to function as intended. For most reward values ranging from -0.4 to -0.9 , the algorithm consistently reached the maximum number of angles. As shown in Figure (5), the negative reward setting of -0.5 yielded different numbers of angles for each shape, whereas the -0.6 setting failed to produce valid results. This outcome indicates that the policy gradient lacked robustness, failed to converge reliably in the intended direction, and tended to ignore the terminal action.

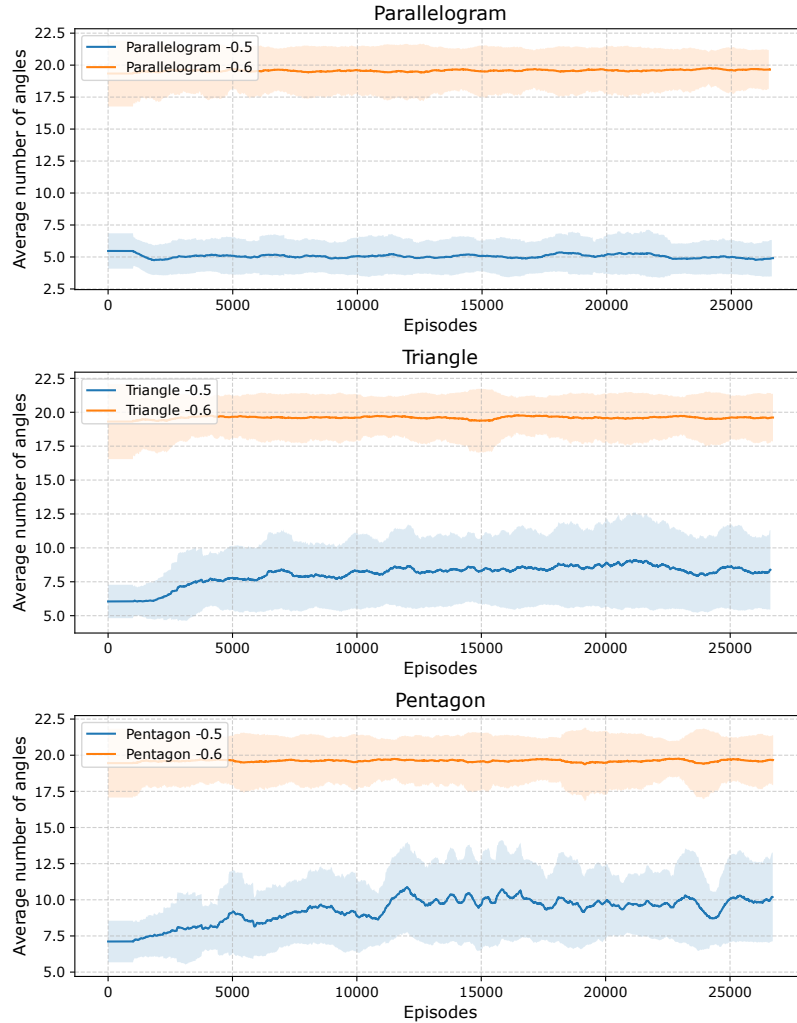


Figure 5: Comparison of the number of angles selected by the naive policy and by negative reward settings of -0.5 and -0.6 . The curves represent the mean number of angles during training, averaged over every 1000 episodes, and the shaded regions indicate the variance. Results are grouped by shape: parallelogram, triangle, and pentagon.

In contrast, the terminal policy remained robust under different reward settings. Figure (6) shows that, during training, the number of angles increased, and more complex shapes required more angles. Lower costs (negative reward is -0.5) generally led to a higher number of angles.

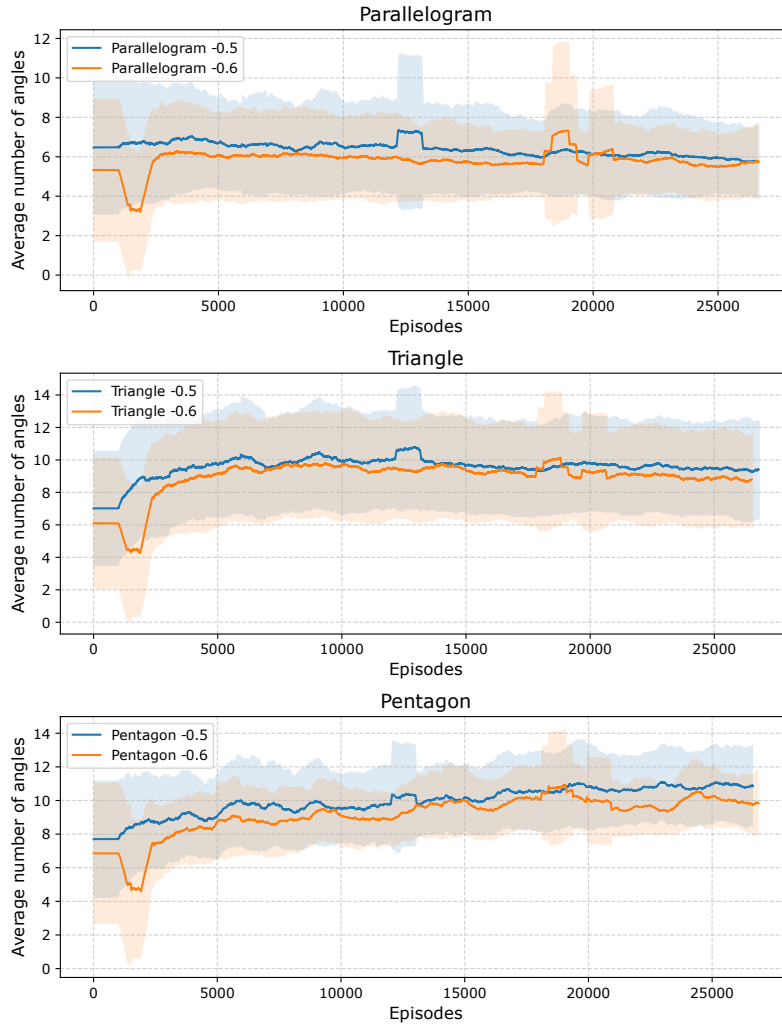


Figure 6: Comparison of the number of angles selected by the terminal policy and by negative reward settings of -0.5 and -0.6 . The curves represent the mean number of angles during training, averaged over every 1000 episodes, and the shaded regions indicate the variance. Results are grouped by shape: parallelogram, triangle, and pentagon.

5.4 Validation on unseen rotations and noise levels

To assess the generalizability of Algorithm (2) for optimal stopping, we applied the policy trained in the previous experiment (which involved 5% Gaussian noise) to synthetic data featuring unseen rotations—rotations not included in the training set shown in Figure (3)—as well as two additional

noise levels: 3% and 7% Gaussian noise. The total number of unseen phantoms was 1,800, with 600 for each shape.

A standard baseline approach, the *Golden Ratio Policy* [34, 35], is considered for comparison with the RL policy. The golden ratio, approximately 1.618, is an irrational number used to guide non-uniform angle selection. Unlike the equidistant policy, this approach retains previously selected angles and adds new angles dynamically. New angles are placed in the largest existing gap between angles, based on the golden ratio. This strategy ensures that the angular distribution adapts while optimizing coverage.

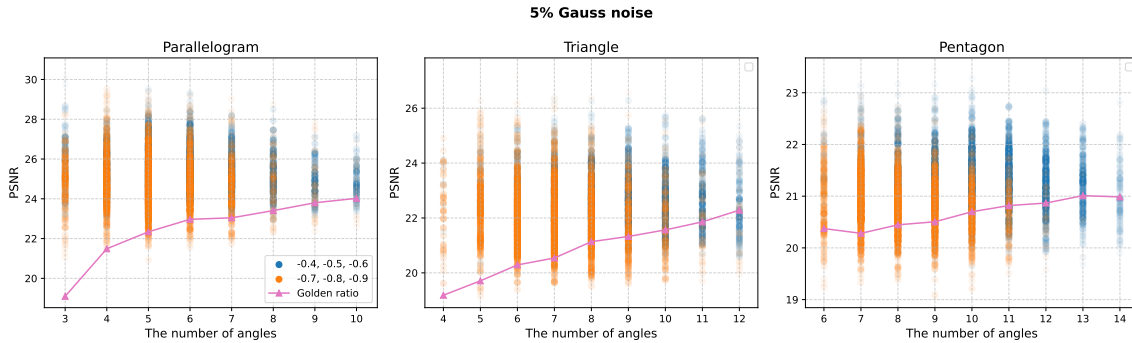


Figure 7: Simulation results are categorized into parallelogram, triangle, and pentagon shapes to illustrate how the number of angles influences PSNR under various rewards and various noise levels. Data points are color-coded by negative reward values—blue ($-0.4, -0.5, -0.6$) and orange ($-0.7, -0.8, -0.9$). Increased transparency indicates data points that are further from the mean. Triangular markers represent the mean PSNR values obtained from the golden ratio policy at each corresponding angle.

Figure (10) shows the validation results for negative rewards ranging from -0.4 to -0.9 (in increments of 0.1) under Gaussian noise level of 5%. Results for Gaussian noise levels of 3% and 7% are presented in Appendix C. Each data point represents the relationship between the number of angles and the corresponding PSNR value. For clarity, results are grouped by shape (parallelogram, triangle, and pentagon). The Golden Ratio policy used the same synthetic data with unseen rotations and the same number of angles chosen by the terminal policy. For each number of angles used by the Golden Ratio policy, the mean PSNR value was calculated.

Overall, the RL approach with the terminal policy achieved higher PSNR values compared to the Golden Ratio policy. At lower numbers of angles, the Golden Ratio policy consistently produced lower mean PSNR values across all shapes, with the difference between the two methods diminishing as the number of angles increased. As shape complexity increased from parallelogram to pentagon, the performance gap between the two policies narrowed. For instance, at lower numbers of angles for the parallelogram, the RL approach yielded data points above the mean value of the Golden Ratio policy, while for the more complex pentagon shape, the RL policy’s advantage was less pronounced. Figure (10) uses distinct colors to represent different ranges of negative reward values, with generally lower experimental costs leading to fewer angles. As experimental cost increases, the number of angles decreases across all shapes. In Figure (10), the orange points (indicating higher costs) are concentrated at lower numbers of angles, while the blue points (indicating lower costs) are found at higher numbers of angles; however, the distinction is more evident for complex shapes, which require more angles.

Table 1: Comparison of the number of angles and PSNR values for triangle and pentagon shapes under different noise levels.

Shape	Noise	The number of angles	RL (PSNR)	Golden ratio (PSNR)
Parallelogram	3%	6.02 ± 2.26	25.96 ± 1.29	22.65 ± 2.17
Parallelogram	5%	6.96 ± 2.81	25.55 ± 1.10	22.92 ± 2.06
Parallelogram	7%	9.41 ± 3.98	24.99 ± 0.95	23.21 ± 1.91
Triangle	3%	8.54 ± 1.97	23.42 ± 1.10	21.58 ± 1.71
Triangle	5%	9.43 ± 2.21	22.85 ± 1.09	21.44 ± 1.54
Triangle	7%	11.39 ± 3.09	22.05 ± 1.12	21.17 ± 1.41
Pentagon	3%	10.43 ± 1.98	22.66 ± 0.67	22.21 ± 0.51
Pentagon	5%	10.99 ± 2.01	21.47 ± 0.56	20.99 ± 0.51
Pentagon	7%	12.56 ± 2.25	20.01 ± 0.58	19.56 ± 0.52

Table (1) summarizes the number of angles selected for the three shapes during validation under different noise levels, with the negative reward fixed at -0.5 . In general, lower noise levels lead to fewer angles being chosen. As shown in the table, each shape requires the fewest angles at 3% Gaussian noise, whereas 7% Gaussian noise leads to the largest number of angles. Furthermore, the number of angles increases with the complexity of the geometry: the parallelogram requires the fewest angles, while the pentagon requires the most.

5.5 Test on real data with two noise levels

We explored the gap between simulation and the real world by applying the model trained on the synthetic dataset to the real data described in Section 5.1.2. Building on the potential demonstrated in the simulation, we further investigated whether the trained model could adapt to changes in the real scanning environment, particularly variations in noise levels. Two noise levels were considered, based on different emission current settings ($600 \mu\text{A}$ and $100 \mu\text{A}$). The model was trained using 5% Gaussian noise on the projections, while the noise in the real data typically consists of a mixture of Poisson and Gaussian noise [36]. It is important to demonstrate whether training under simplified conditions (Gaussian noise model) can produce reasonable results when applied to the more complex conditions of the real world (real noise model).

Figure (8) shows results obtained from real data using three trained models under varying emission currents and reward settings. The Golden Ratio policy used the same number of angles chosen by the terminal policy. For each number of angles used by the Golden Ratio policy, the mean PSNR value was calculated. Several consistent trends emerged across the 12 data groups, aligning with the conclusions from the validation. First, pentagon data points generally involved a larger number of angles than triangles. Second, noisier data from the lower emission current ($100 \mu\text{A}$) tended to require more angles than data collected at the higher emission current ($600 \mu\text{A}$). Third, although the number of samples was limited, it was still evident that lower experimental costs (e.g., -0.4 , -0.5 and -0.6) led to more angles, while higher costs (e.g., -0.7 , -0.8 and -0.9) required fewer angles. Finally, the RL policy clearly outperformed the Golden Ratio policy when fewer angles were selected, though the difference between them diminished as the number of angles increased.

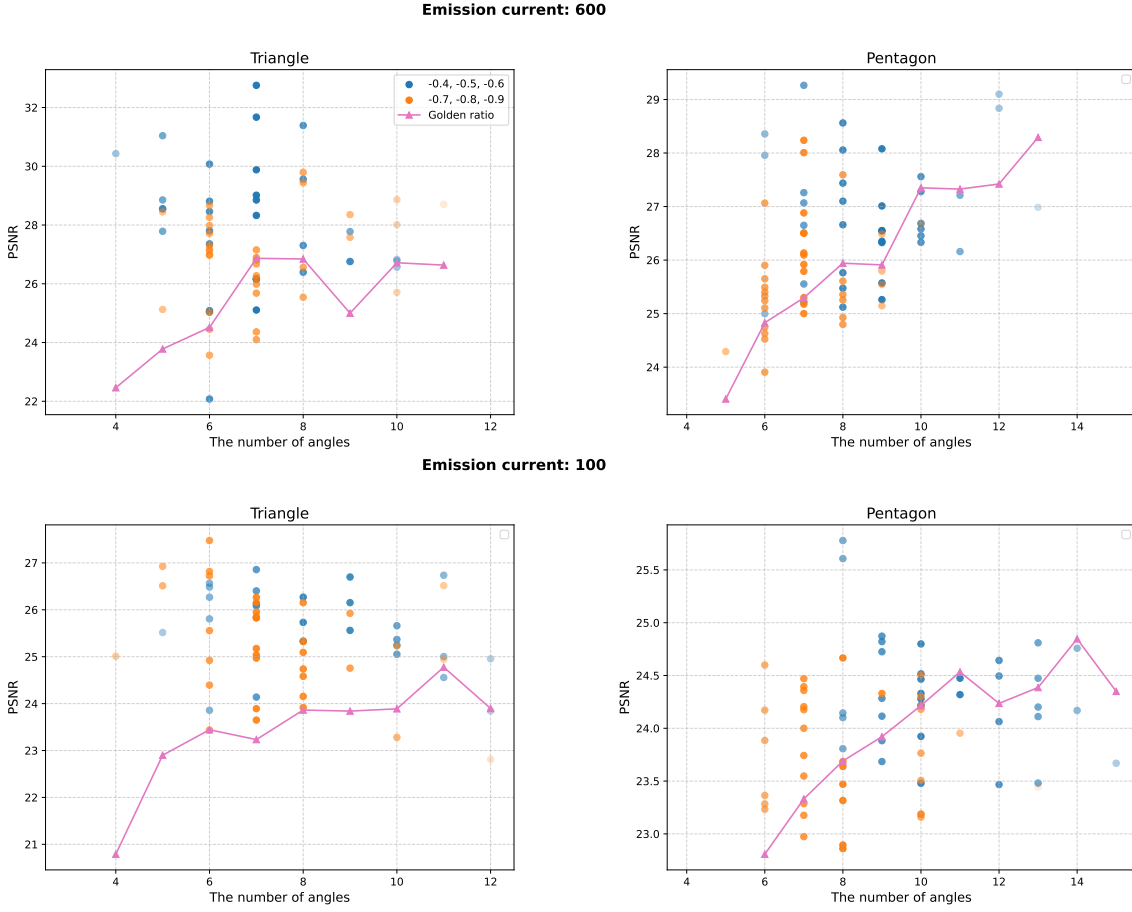


Figure 8: Results on real data for the triangle and pentagon shapes are shown, illustrating how the number of angles affects PSNR under various negative rewards and noise levels. Data points are color-coded by their negative reward values: blue ($-0.4, -0.5, -0.6$) and orange ($-0.7, -0.8, -0.9$). Triangular markers represent the mean PSNR values obtained from the Golden Ratio policy at each corresponding number of angles.

To evaluate reconstruction quality, we used the reconstruction obtained with all 180 angles as the ground truth. Table (2) compares the performance of the RL policy and baseline policies under an emission current of 600 μA and 100 μA under a reward setting of -0.5 . The RL policy consistently outperformed the Golden Ratio policy for triangles, while it was only comparable to the baselines for pentagons. This outcome, likely influenced by the gap between simulation and real-world data, is consistent with the training results, where the RL policy did not demonstrate a particularly distinct advantage for pentagon shapes.

Additionally, Figure (9) illustrates sample reconstructions for the three policies, with the number of angles determined by the RL policy. The results show that the angles selected by the RL policy tend to cluster around the edges. Furthermore, as the noise level increases (from an emission current of 600 μA to 100 μA), the number of selected angles increases, and their distribution becomes broader.

Table 2: Comparison of the number of angles and PSNR values for triangle and pentagon shapes under two different noise levels.

Shape	Noise	The number of angles	RL (PSNR)	Golden ratio (PSNR)
Triangle	600	7.92 ± 3.04	27.38 ± 2.09	25.58 ± 2.10
Triangle	100	11.08 ± 2.87	25.95 ± 0.72	24.47 ± 1.32
Pentagon	600	9.17 ± 1.86	26.63 ± 1.13	26.84 ± 0.87
Pentagon	100	10.33 ± 2.05	24.50 ± 0.63	24.40 ± 0.30

Consequently, the RL policy trained on simulation data with a simple Gaussian noise model demonstrated reasonable performance on real data, effectively handling both optimal stopping and the selection of informative angles.

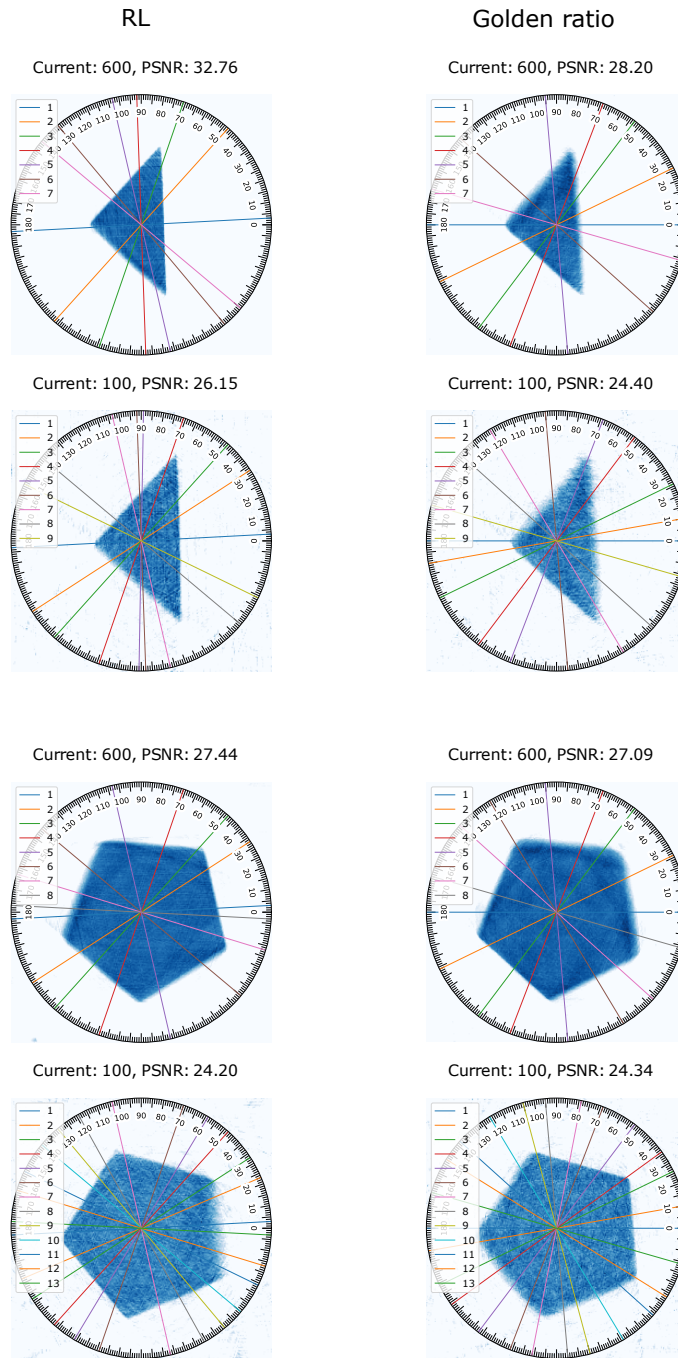


Figure 9: Reconstruction samples on real data under emission current $100 \mu\text{A}$ and $600 \mu\text{A}$ for -0.6 reward.

6 Discussion

These results demonstrate that our algorithm effectively balances experimental costs and reconstruction quality by incorporating optimal stopping and adaptively selecting informative angles through deep reinforcement learning. Moreover, the model trained on a synthetic dataset with a simple Gaussian noise model showed satisfactory performance on real-world data, which typically includes more complex noise, such as a mixture of Gaussian and Poisson noise. The algorithm also demonstrated its ability to adapt the number of angles (optimal stopping) to varying noise levels in real-world scenarios while maintaining a consistent level of experimental quality.

Despite these encouraging findings, several areas for improvement remain. First, the gap between simulation and real-world performance could be minimized by incorporating more realistic simulators that account for precise noise models. Second, the training process could be improved by adopting a multi-stage approach, where the model is initially trained on simulated data and subsequently fine-tuned using real-world data. Third, extending the dataset to three-dimensional scenarios would enable the exploration of larger action and state spaces, further enhancing the model's capability. Additionally, task-specific zooming techniques could be integrated for applications such as defect detection. Finally, incorporating learning-based reconstruction algorithms could facilitate the extraction of informative features directly from the reconstruction process, providing a more robust basis for selecting informative angles.

7 Conclusion

In this paper, we proposed an approach to simultaneously optimize adaptive informative angle selection and optimal stopping by introducing a terminal policy and jointly computing the policy gradient for both the angle selection and terminal policies. Additionally, we investigated the gap between simulation and real-world scenarios. Our findings demonstrate the feasibility of achieving optimal stopping for sequential OED based on experimental costs. Furthermore, the trained model from simulation showed promising potential for application to real-world data, highlighting its value for industrial CT applications. This approach paves the way for fully adaptive scanning processes, optimizing both the selection of informative angles and the number of angles required.

8 Acknowledgement

This research was co-financed by the European Union H2020-MSCA-ITN-2020 under grant agreement no. 956172 (xCTing).

References

- [1] I. Kazantsev, "Information content of projections," *Inverse problems*, vol. 7, no. 6, p. 887, 1991.
- [2] L. Varga, P. Balázs, and A. Nagy, "Projection selection dependency in binary tomography," *Acta Cybernetica*, vol. 20, no. 1, pp. 167–187, 2011.
- [3] D. V. Lindley, *Bayesian statistics: A review*. SIAM, 1972.
- [4] K. Chaloner and I. Verdinelli, "Bayesian experimental design: A review," *Statistical science*, pp. 273–304, 1995.

- [5] T. Rainforth, A. Foster, D. R. Ivanova, and F. Bickford Smith, “Modern bayesian experimental design,” *Statistical Science*, vol. 39, no. 1, pp. 100–114, 2024.
- [6] K. J. Batenburg, W. J. Palenstijn, P. Balázs, and J. Sijbers, “Dynamic angle selection in binary tomography,” *Computer Vision and Image Understanding*, vol. 117, no. 4, pp. 306–318, 2013.
- [7] A. Dabrovolski, K. J. Batenburg, and J. Sijbers, “Dynamic angle selection in X-ray computed tomography,” *Nuclear Instruments and Methods in Physics Research Section B: Beam Interactions with Materials and Atoms*, vol. 324, pp. 17–24, 2014.
- [8] K. J. Batenburg, W. Fortes, L. Hajdu, and R. Tjeldeman, “Bounds on the difference between reconstructions in binary tomography,” in *International Conference on Discrete Geometry for Computer Imagery*. Springer, 2011, pp. 369–380.
- [9] M. Burger, A. Hauptmann, T. Helin, N. Hyvönen, and J.-P. Puska, “Sequentially optimized projections in X-ray imaging,” *Inverse Problems*, vol. 37, no. 7, p. 075006, 2021.
- [10] X. Huan, J. Jagalur, and Y. Marzouk, “Optimal experimental design: Formulations and computations,” *Acta Numerica*, vol. 33, pp. 715–840, 2024.
- [11] T. Helin, N. Hyvönen, and J.-P. Puska, “Edge-promoting adaptive bayesian experimental design for X-ray imaging,” *SIAM Journal on Scientific Computing*, vol. 44, no. 3, pp. B506–B530, 2022.
- [12] R. Barbano, J. Leuschner, J. Antorán, B. Jin, and J. M. Hernández-Lobato, “Bayesian experimental design for computed tomography with the linearised deep image prior,” *arXiv preprint arXiv:2207.05714*, 2022.
- [13] N. Elata, T. Michaeli, and M. Elad, “Adaptive compressed sensing with diffusion-based posterior sampling,” in *European Conference on Computer Vision*. Springer, 2025, pp. 290–308.
- [14] W. Shen and X. Huan, “Bayesian sequential optimal experimental design for nonlinear models using policy gradient reinforcement learning,” *Computer Methods in Applied Mechanics and Engineering*, vol. 416, p. 116304, 2023.
- [15] T. Blau, E. V. Bonilla, I. Chades, and A. Dezfouli, “Optimizing sequential experimental design with deep reinforcement learning,” in *International conference on machine learning*. PMLR, 2022, pp. 2107–2128.
- [16] A. Foster, D. R. Ivanova, I. Malik, and T. Rainforth, “Deep adaptive design: Amortizing sequential bayesian experimental design,” in *International conference on machine learning*. PMLR, 2021, pp. 3384–3395.
- [17] Z. Shen, Y. Wang, D. Wu, X. Yang, and B. Dong, “Learning to scan: A deep reinforcement learning approach for personalized scanning in CT imaging,” *Inverse Problems & Imaging*, vol. 16, no. 1, 2022.
- [18] T. Wang, F. Lucka, and T. van Leeuwen, “Sequential experimental design for x-ray ct using deep reinforcement learning,” *IEEE Transactions on Computational Imaging*, vol. 10, pp. 953–968, 2024.
- [19] T. Wang, V. Florian, R. Schielein, C. Kretzer, S. Kasperl, F. Lucka, and T. van Leeuwen, “Task-adaptive angle selection for computed tomography-based defect detection,” *Journal of Imaging*, vol. 10, no. 9, p. 208, 2024.

- [20] J. L. Mueller and S. Siltanen, *Linear and nonlinear inverse problems with practical applications*. SIAM, 2012.
- [21] E. Ryan, C. Drovandi, J. McGree, and A. Pettitt, “Fully bayesian optimal experimental design: A review,” *International Statistical Review*, vol. 84, pp. 128–154, 2016.
- [22] L. Ruthotto, J. Chung, and M. Chung, “Optimal experimental design for inverse problems with state constraints,” *SIAM Journal on Scientific Computing*, vol. 40, no. 4, pp. B1080–B1100, 2018.
- [23] R. S. Sutton and A. G. Barto, *Reinforcement learning: An introduction*. MIT press, 2018.
- [24] P.-L. Bacon, J. Harb, and D. Precup, “The option-critic architecture,” in *Proceedings of the AAAI conference on artificial intelligence*, vol. 31, no. 1, 2017.
- [25] N. Damera Venkata and C. Bhattacharyya, “Deep recurrent optimal stopping,” *Advances in Neural Information Processing Systems*, vol. 36, 2024.
- [26] G. Peskir and A. Shiryaev, *Optimal stopping and free-boundary problems*. Springer, 2006.
- [27] S. Becker, P. Cheridito, and A. Jentzen, “Deep optimal stopping,” *Journal of Machine Learning Research*, vol. 20, no. 74, pp. 1–25, 2019.
- [28] D. Pollard, “Optimal stopping,” <http://www.stat.yale.edu/~pollard/Courses/251.spring2013/Handouts/optimal.pdf>, 2013, course handout for STAT 251 at Yale University. [Online]. Available: <http://www.stat.yale.edu/~pollard/Courses/251.spring2013/Handouts/optimal.pdf>
- [29] W. Van Aarle, W. J. Palenstijn, J. De Beenhouwer, T. Altantzis, S. Bals, K. J. Batenburg, and J. Sijbers, “The astra toolbox: A platform for advanced algorithm development in electron tomography,” *Ultramicroscopy*, vol. 157, pp. 35–47, 2015.
- [30] W. Van Aarle, W. J. Palenstijn, J. Cant, E. Janssens, F. Bleichrodt, A. Dabravolski, J. De Beenhouwer, K. Joost Batenburg, and J. Sijbers, “Fast and flexible x-ray tomography using the astra toolbox,” *Optics express*, vol. 24, no. 22, pp. 25 129–25 147, 2016.
- [31] T. Wang, F. Lucka, and T. van Leeuwen, “X-ray computed tomography case study: Triangle and pentagon datasets with various sizes, scales, and noise levels,” Feb. 2025. [Online]. Available: <https://doi.org/10.5281/zenodo.14893740>
- [32] Z. Jin, H.-M. Zhang, B. Yan, L. Li, L.-Y. Wang, and A.-L. Cai, “Novel fourier-based iterative reconstruction for sparse fan projection using alternating direction total variation minimization,” *Chinese Physics B*, vol. 25, no. 3, p. 038701, 2016.
- [33] D. P. Kingma, “Adam: A method for stochastic optimization,” *arXiv preprint arXiv:1412.6980*, 2014.
- [34] T. Kohler, “A projection access scheme for iterative reconstruction based on the golden section,” in *IEEE Symposium Conference Record Nuclear Science 2004.*, vol. 6. IEEE, 2004, pp. 3961–3965.
- [35] T. M. Craig, A. A. Kadu, K. J. Batenburg, and S. Bals, “Real-time tilt undersampling optimization during electron tomography of beam sensitive samples using golden ratio scanning and recast3d,” *Nanoscale*, vol. 15, no. 11, pp. 5391–5402, 2023.

- [36] V. Andriashen, R. van Liere, T. van Leeuwen, and K. J. Batenburg, “X-ray image generation as a method of performance prediction for real-time inspection: a case study,” *Journal of Nondestructive Evaluation*, vol. 43, no. 3, p. 79, 2024.

A Policy gradient on w_a

The following equations show the relationships between the continuation state-value function and the continuation action-value function according to Equation (2) and Equation (5):

$$V_C^{\pi_a, \pi_t}(\hat{\mathbf{x}}) = \sum_{\theta} \pi_{\text{action}}(\theta | \hat{\mathbf{x}}; \mathbf{w}_a) Q_C^{\pi_a, \pi_t}(\hat{\mathbf{x}}, \theta) \quad (17)$$

$$Q_C^{\pi_a, \pi_t}(\hat{\mathbf{x}}, \theta) = -b + \sum_{\hat{\mathbf{x}}'} \pi_t(\hat{\mathbf{x}}' | \hat{\mathbf{x}}, \theta) V^{\pi_a, \pi_t}(\hat{\mathbf{x}}') \quad (18)$$

Advantage function A : It is used to evaluate if the selected action is better than average performance at the current state:

$$\begin{aligned} A_C^{\pi_a, \pi_t}(\hat{\mathbf{x}}, \theta) &= \underbrace{Q_C^{\pi_a, \pi_t}(\hat{\mathbf{x}}, \theta)}_{Q_C^{\pi_a, \pi_t} \rightarrow V_C^{\pi_a, \pi_t}: \text{Equation (18)}} - \underbrace{\sum_{\theta} \pi_{\text{action}}(\theta | \hat{\mathbf{x}}; \mathbf{w}_a) Q_C^{\pi_a, \pi_t}(\hat{\mathbf{x}}, \theta)}_{V_C^{\pi_a, \pi_t} \rightarrow Q_C^{\pi_a, \pi_t}: \text{Equation (17)}} \\ &= -b + \underbrace{\sum_{\hat{\mathbf{x}}'} \pi_t(\hat{\mathbf{x}}' | \hat{\mathbf{x}}, \theta) V^{\pi_a, \pi_t}(\hat{\mathbf{x}}')}_{\text{involve terminal policy: Equation (9)}} - V_C^{\pi_a, \pi_t}(\hat{\mathbf{x}}) \\ &= -b + \sum_{\hat{\mathbf{x}}'} \pi_t(\hat{\mathbf{x}}' | \hat{\mathbf{x}}, \theta) \left((1 - \pi_{\text{ter}}(d' | \hat{\mathbf{x}}'; \mathbf{w}_t)) V_C^{\pi_a, \pi_t}(\hat{\mathbf{x}}') + \pi_{\text{ter}}(d' | \hat{\mathbf{x}}'; \mathbf{w}_t) \text{PSNR}(\hat{\mathbf{x}}', \bar{\mathbf{x}}) \right) \\ &\quad - V_C^{\pi_a, \pi_t}(\hat{\mathbf{x}}) \\ &\text{sample } \hat{\mathbf{x}}' \text{ from } \pi_t, \text{ because we do not know the model } \pi_t \\ &\approx -b + (1 - \pi_{\text{ter}}(d' | \hat{\mathbf{x}}'; \mathbf{w}_t)) V_C^{\pi_a, \pi_t}(\hat{\mathbf{x}}') + \pi_{\text{ter}}(d' | \hat{\mathbf{x}}'; \mathbf{w}_t) \text{PSNR}(\hat{\mathbf{x}}', \bar{\mathbf{x}}) - V_C^{\pi_a, \pi_t}(\hat{\mathbf{x}}). \end{aligned} \quad (19)$$

$$\begin{aligned}
\nabla_{\mathbf{w}_a} J(\mathbf{w}_a, \mathbf{w}_t) &= \underbrace{\nabla_{\mathbf{w}_a} V^{\pi_a, \pi_t}(\hat{\mathbf{x}}_1)}_{\text{involve terminal policy: Equation (9)}} \\
&= \nabla_{\mathbf{w}_a} \left(\pi_{\text{ter}}(d_1 | \hat{\mathbf{x}}_1; \mathbf{w}_t) \text{PSNR}(\hat{\mathbf{x}}_1, \bar{\mathbf{x}}) + \left(1 - \pi_{\text{ter}}(d_1 | \hat{\mathbf{x}}_1; \mathbf{w}_t)\right) V_C^{\pi_a, \pi_t}(\hat{\mathbf{x}}_1) \right) \\
&= \left(1 - \pi_{\text{ter}}(d_1 | \hat{\mathbf{x}}_1; \mathbf{w}_t)\right) \nabla_{\mathbf{w}_a} \underbrace{V_C^{\pi_a, \pi_t}(\hat{\mathbf{x}}_1)}_{V_C^{\pi_a, \pi_t} \rightarrow Q_C^{\pi_a, \pi_t}: \text{Equation (17)}} \\
&= \left(1 - \pi_{\text{ter}}(d_1 | \hat{\mathbf{x}}_1; \mathbf{w}_t)\right) \left(\sum_{\theta} \nabla_{\mathbf{w}_a} \pi_{\text{action}}(\theta | \hat{\mathbf{x}}_1; \mathbf{w}_a) Q_C^{\pi_a, \pi_t}(\hat{\mathbf{x}}_1, \theta) \right. \\
&\quad \left. + \sum_{\theta} \pi_{\text{action}}(\theta | \hat{\mathbf{x}}_1; \mathbf{w}_a) \nabla_{\mathbf{w}_a} \underbrace{Q_C^{\pi_a, \pi_t}(\hat{\mathbf{x}}_1, \theta)}_{Q_C^{\pi_a, \pi_t} \rightarrow V_C^{\pi_a, \pi_t}: \text{Equation (18)}} \right) \\
&= \left(1 - \pi_{\text{ter}}(d_1 | \hat{\mathbf{x}}_1; \mathbf{w}_t)\right) \left(\sum_{\theta} \nabla_{\mathbf{w}_a} \pi_{\text{action}}(\theta | \hat{\mathbf{x}}_1; \mathbf{w}_a) Q_C^{\pi_a, \pi_t}(\hat{\mathbf{x}}_1, \theta) \right. \\
&\quad \left. + \sum_{\theta} \pi_{\text{action}}(\theta | \hat{\mathbf{x}}_1; \mathbf{w}_a) \sum_{\hat{\mathbf{x}}} \pi_t(\hat{\mathbf{x}} | \hat{\mathbf{x}}_1, \theta) \underbrace{\nabla_{\mathbf{w}_a} V^{\pi_a, \pi_t}(\hat{\mathbf{x}})}_{\text{unrolling recursive derivation}} \right)
\end{aligned} \tag{20}$$

After the unrolling recursive derivation,

$$\begin{aligned}
\nabla_{\mathbf{w}_a} J(\mathbf{w}_a, \mathbf{w}_t) &= \nabla_{\mathbf{w}_a} V^{\pi_a, \pi_t}(\hat{\mathbf{x}}_1) \\
&= \sum_{k=1}^T \sum_{\theta, \hat{\mathbf{x}}} \pi_1^{(k)}(\theta, \hat{\mathbf{x}}, d_{k+1} | \hat{\mathbf{x}}_k; \mathbf{w}_a, \mathbf{w}_t) \sum_{\theta'} \nabla_{\mathbf{w}_a} \pi_{\text{action}}(\theta' | \hat{\mathbf{x}}_k; \mathbf{w}_a) Q_C^{\pi_a, \pi_t}(\hat{\mathbf{x}}, \theta') \\
&= \sum_{k=1}^T \sum_{\theta, \hat{\mathbf{x}}} \pi_1^{(k)}(\theta, \hat{\mathbf{x}}, d_{k+1} | \hat{\mathbf{x}}_k; \mathbf{w}_a, \mathbf{w}_t) \\
&\quad \sum_{\theta'} \pi_{\text{action}}(\theta' | \hat{\mathbf{x}}_k; \mathbf{w}_a) \underbrace{\frac{\nabla_{\mathbf{w}_a} \pi_{\text{action}}(\theta' | \hat{\mathbf{x}}_k; \mathbf{w}_a)}{\pi_{\text{action}}(\theta' | \hat{\mathbf{x}}_k; \mathbf{w}_a)}}_{\nabla_{\mathbf{w}_a} \log \pi_{\text{action}}(\theta' | \hat{\mathbf{x}}_k; \mathbf{w}_a)} Q_C^{\pi_a, \pi_t}(\hat{\mathbf{x}}, \theta'),
\end{aligned} \tag{21}$$

where

$$\pi_1^{(k)}(\theta, \hat{\mathbf{x}}, d_{k+1} | \hat{\mathbf{x}}_k; \mathbf{w}_a, \mathbf{w}_t) = \begin{cases} \sum_{\theta} \pi_{\text{action}}(\theta | \hat{\mathbf{x}}_k; \mathbf{w}_a) \sum_{\hat{\mathbf{x}}} \pi_t(\hat{\mathbf{x}} | \hat{\mathbf{x}}_k, \theta) \left(1 - \pi_{\text{ter}}(d_{k+1} | \hat{\mathbf{x}}; \mathbf{w}_t)\right), & \text{if } k \neq 0, \\ \left(1 - \pi_{\text{ter}}(d_{k+1} | \hat{\mathbf{x}}_{k+1}; \mathbf{w}_t)\right), & \text{if } k = 0. \end{cases}$$

B Policy gradient on \mathbf{w}_t

$$\begin{aligned}
\nabla_{\mathbf{w}_t} J(\mathbf{w}_a, \mathbf{w}_t) &= \underbrace{\nabla_{\mathbf{w}_t} V^{\pi_a, \pi_t}(\hat{\mathbf{x}}_1)}_{\text{involve terminal policy: Equation (9)}} \\
&= \nabla_{\mathbf{w}_t} \left(\pi_{\text{ter}}(d_1 | \hat{\mathbf{x}}_1; \mathbf{w}_t) \text{PSNR}(\hat{\mathbf{x}}_1, \bar{\mathbf{x}}) + \left(1 - \pi_{\text{ter}}(d_1 | \hat{\mathbf{x}}_1; \mathbf{w}_t)\right) V_C^{\pi_a, \pi_t}(\hat{\mathbf{x}}_1) \right) \\
&= \nabla_{\mathbf{w}_t} \pi_{\text{ter}}(d_1 | \hat{\mathbf{x}}_1; \mathbf{w}_t) \text{PSNR}(\hat{\mathbf{x}}_1, \bar{\mathbf{x}}) \\
&\quad - \nabla_{\mathbf{w}_t} \pi_{\text{ter}}(d_1 | \hat{\mathbf{x}}_1; \mathbf{w}_t) V_C^{\pi_a, \pi_t}(\hat{\mathbf{x}}_1) + \left(1 - \pi_{\text{ter}}(d_1 | \hat{\mathbf{x}}_1; \mathbf{w}_t)\right) \nabla_{\mathbf{w}_t} \underbrace{V_C^{\pi_a, \pi_t}(\hat{\mathbf{x}}_1)}_{V_C^{\pi_a, \pi_t} \rightarrow Q_C^{\pi_a, \pi_t}: \text{Equation (17)}} \\
&= \nabla_{\mathbf{w}_t} \pi_{\text{ter}}(d_1 | \hat{\mathbf{x}}_1; \mathbf{w}_t) \left(\text{PSNR}(\hat{\mathbf{x}}_1, \bar{\mathbf{x}}) - V_C^{\pi_a, \pi_t}(\hat{\mathbf{x}}_1) \right) \\
&\quad + \left(1 - \pi_{\text{ter}}(d_1 | \hat{\mathbf{x}}_1; \mathbf{w}_t)\right) \sum_{\theta} \pi_{\text{action}}(\theta | \hat{\mathbf{x}}_1; \mathbf{w}_a) \nabla_{\mathbf{w}_t} \underbrace{Q_C^{\pi_a, \pi_t}(\hat{\mathbf{x}}_1, \theta)}_{Q_C^{\pi_a, \pi_t} \rightarrow V_C^{\pi_a, \pi_t}: \text{Equation (18)}} \\
&= \nabla_{\mathbf{w}_t} \pi_{\text{ter}}(d_1 | \hat{\mathbf{x}}_1; \mathbf{w}_t) \left(\text{PSNR}(\hat{\mathbf{x}}_1, \bar{\mathbf{x}}) - V_C^{\pi_a, \pi_t}(\hat{\mathbf{x}}_1) \right) \\
&\quad + \left(1 - \pi_{\text{ter}}(d_1 | \hat{\mathbf{x}}_1; \mathbf{w}_t)\right) \sum_{\theta} \pi_{\text{action}}(\theta | \hat{\mathbf{x}}_1; \mathbf{w}_a) \sum_{\hat{\mathbf{x}}} \pi_t(\hat{\mathbf{x}} | \hat{\mathbf{x}}_1, \theta) \underbrace{\nabla_{\mathbf{w}_t} V^{\pi_a, \pi_t}(\hat{\mathbf{x}})}_{\text{unrolling recursive derivation}} \\
&\hspace{15em} (22)
\end{aligned}$$

After the unrolling recursive derivation,

$$\begin{aligned}
\nabla_{\mathbf{w}_t} J(\mathbf{w}_a, \mathbf{w}_t) &= \nabla_{\mathbf{w}_t} V^{\pi_a, \pi_t}(\hat{\mathbf{x}}) \\
&= \sum_{k=1}^T \sum_{\theta, \hat{\mathbf{x}}} \pi_2^{(k)}(\theta, \hat{\mathbf{x}}, d_k | \hat{\mathbf{x}}_k; \mathbf{w}_a, \mathbf{w}_t) \nabla_{\mathbf{w}_t} \pi_{\text{ter}}(d | \hat{\mathbf{x}}; \mathbf{w}_t) \left(\text{PSNR}(\hat{\mathbf{x}}, \bar{\mathbf{x}}) - V_C^{\pi_a, \pi_t}(\hat{\mathbf{x}}) \right), \\
&\hspace{15em} (23)
\end{aligned}$$

where

$$\pi_2^{(k)}(\theta, \hat{\mathbf{x}}, d_k | \hat{\mathbf{x}}_k; \mathbf{w}_a, \mathbf{w}_t) = \begin{cases} \left(1 - \pi_{\text{ter}}(d_k | \hat{\mathbf{x}}_k; \mathbf{w}_t)\right) \sum_{\theta} \pi_{\text{action}}(\theta | \hat{\mathbf{x}}_k; \mathbf{w}_a) \sum_{\hat{\mathbf{x}}} \pi_t(\hat{\mathbf{x}} | \hat{\mathbf{x}}_k, \theta), & \text{if } k \neq 0, \\ 1, & \text{if } k = 0. \end{cases}$$

C Additional results

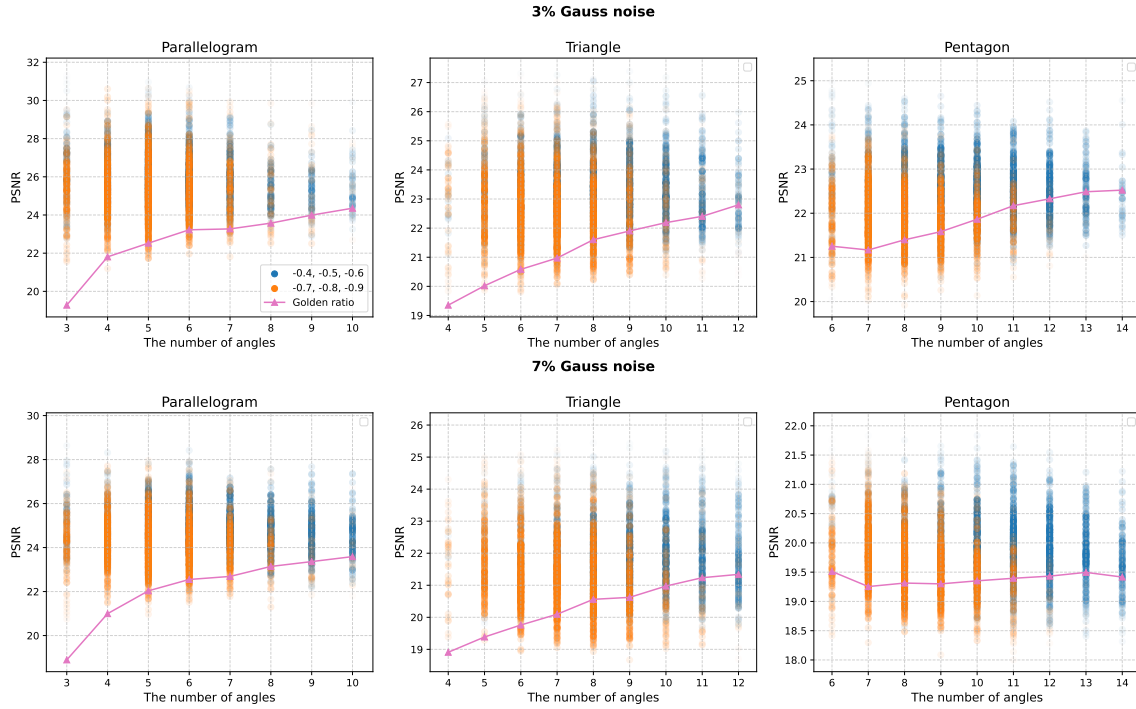


Figure 10: Simulation results are categorized into parallelogram, triangle, and pentagon shapes to illustrate how the number of angles influences PSNR under various rewards and various noise levels. Data points are color-coded by negative reward values—blue ($-0.4, -0.6$) and orange ($-0.7, -0.9$). Increased transparency indicates data points that are further from the mean. Triangular markers represent the mean PSNR values obtained from the golden ratio policy at each corresponding angle.